Volume 12, Year 2025 ISSN: 2564-4998

DOI: 10.11159/jbeb.2025.011

Versatile Laser Ablation System for Cellular Response Analysis

Sophia Liu^{1,†}, David Z. He^{1,†}, Veronica Gomez-Godinez¹, Zachary Wang¹, Chengbiao Wu², Linda Shi^{1*}

¹University of California, San Diego, Institute of Engineering in Medicine, 9500 Gilman Dr, La Jolla, California, USA, 92093

slliu0129@gmail.com; davidzhanghe258@gmail.com; gomezvg@gmail.com; zaw001@ucsd.edu ²University of California, San Diego, Department of Neurosciences, 9500 Gilman Dr, La Jolla, CA, USA, 92093 chw049@health.ucsd.edu

†High school students participating in IEM OPALS program, equally contributed *Correspondence: zshi@ucsd.edu

Abstract - Femtosecond laser ablation creates precise microinjuries that reveal how cells respond to damage linked to degenerative disease. A Robotic Laser Microscope (Robolase) setup, combined with fluorescence imaging and quantitative phase imaging (QPI), was applied across six new area of studies: primary mouse cortical neurons, cardiomyocytes, rat pheochromocytoma (PC12), human embryonic kidney (HEK293), hippocampal (wild type and Huntington's disease, HD), and retinal ganglion cells (RGCs). In cortical neurons, axonal cuts under normal (3 mM) versus high (25 mM) glucose consistently led to post-ablation retraction, supporting evaluation of axonal robustness under diabetic conditions. In cardiomyocytes, patterned ablation that simulated a loss-ofneighbor border zone produced measurable changes in bordercell area over time. QPI detected power-dependent, real-time thickness shifts in HEK293 and PC12 cells after ablation, providing label-free readouts of subcellular mass redistribution. In hippocampal neurons, HD cultures showed larger axonal separation than wild type; nicotinamide reduced degeneration in a dose-dependent manner, and H_2O_2 modestly increased it. In RGCs, axonal injury triggered rapid axonal Ca²⁺ spikes followed by delayed, larger somatic peaks that decayed over minutes. These results position laser ablation as a practical platform for quantifying structural and signaling dynamics after controlled injury and for screening candidate modulators of degeneration.

Keywords: Femtosecond laser ablation, axonal degeneration, border zone, quantitative phase imaging, calcium imaging, Huntington's disease, retinal ganglion cells

Date Received: 2025-04-08 Date Revised: 2025-09-26 Date Accepted: 2025-10-18 Date Published: 2025-11-25 © Copyright 2025 Authors - This is an Open Access article published under the Creative Commons Attribution License terms (http://creativecommons.org/licenses/by/3.0). Unrestricted use, distribution, and reproduction in any medium are permitted, provided the original work is properly cited.

1. Introduction

Laser ablation was established as a powerful tool with important implications for understanding cellular degeneration and damage. Its versatility was demonstrated across multiple research domains, including investigations of DNA repair in cancer cells, neuronal responses to shear forces, and models of traumatic brain injury, among others [1]. Because femtosecond ablation generates localized DNA damage and replication stress, our platform can be paired with damage-response readouts (ATM-MRE11 priming, BIR activation, 53BP1 loss phenotypes) to quantify pathway-specific rescue or sensitization [2–4]. Building on this foundation, it was proposed that laser ablation could be applied more broadly to studies of cellular degeneration. Building on this foundation, it was proposed that laser ablation could be applied more broadly to studies of cellular degeneration. In this study, laser ablation was employed to four types of cellular degeneration: cortical neuron degeneration with diabetes, cardiomyocyte degeneration, hippocampal changes related to Huntington's Disease, and retinal ganglion cells injury relevant to glaucoma. The work was designed to provide new insights to underscore the efficacy of laser ablation as a tool for investigating degenerative conditions. The precision provided by the robotic laser microscope (RoboLase) system enabled reproducible targeting and flexible experimental designs, and, in combination with fluorescent dyes and image analysis tools such as MATLAB or ImageJ.

Diabetic peripheral neuropathy (DPN), a severe complication of diabetes, was attributed from high glucose-induced nerve injury that caused pain, numbness, and weakness [5]. Using the RoboLase system, the influence of glucose levels on cortical neuron resistance to damage. Similarly, myocardial infarction (MI) led to tissue hypoxia and cell death [6]. Accordingly, the ischemic border zone in mouse cardiomyocytes was examined, with attention to cellular responses consistent with "loss of neighbor" hypothesis [7]. Huntington's disease (HD) was associated with progressive decline of motor, cognitive, and emotional changes in axonal degeneration functions, hippocampal neurons under HD conditions were evaluated in the presence of defined chemical modulators. Glaucoma, characterized by progressive loss of retinal ganglion cells (RGCs) and irreversible blindness, was linked to calcium dysregulation essential for neuronal function [8]. In this context, calciumdependent fluorescence in RGCs was analyzed over time at the incision site and soma using the RoboLase system.

Quantitative Phase Imaging (QPI) was recognized as a label-free, non-destructive method to measure cellular and tissue properties. In parallel, a metasurfaces -- engineered two-dimensional structure composed of subwavelength elements were used to manipulate light at the nanoscale, enabling precise control of phase, amplitude, and polarization [9-12]. As a result, the metasurface-based designs were shown to enhance the QPI stability, reliability, and compactness [13-15]. By quantifying phase shifts in light passing through a sample, QPI enabled visualization and analysis of subtle changes in refractive index that often signaled alterations in cellular structure and function [13].

The QPI application was demonstrated in tracking live cell thickness after laser ablation in PC12 and HEK293 cell lines. Laser-induced cellular manipulation was leveraged to study parameter-response relationships (e.g., power) with the aim of optimizing ablation while minimizing collateral damage. QPI provided a robust readout of laser-induced changes in

cellular structures, which was vital for understanding diseases like scleroderma and systemic sclerosis. These observations indicated that QPI's potential for advancing therapeutic strategies and exploring new applications in biomedical research. Recent clinical and developmental applications continue to validate laser-based sectioning at sub-cellular scales, e.g., laser-assisted microdissection for blastocyst biopsy and downstream sequencing [16]. On the label-free side, metasurface-enabled quantitative phase imaging (QPI) has advanced rapidly, improving stability/compactness and enabling single-shot or dualmode phase capture; a 2025 Moiré metalens reached ~1.3 µm performance with TIE reconstruction [17].

2. Materials & Methods 2.1 RoboLase Set Up

RoboLase, a robotic laser microscope system, utilized a Mai Tai femtosecond laser to carefully ablate cells. The near-infrared laser scissors could be modulated easily in both terms of intensity and spatiotemporal position, allowing surrounding regions to remain untouched. This system interfaced with a Zeiss inverted microscope through a series of reflective coated mirrors, which applied high numerical aperture objectives and light sensitive cameras for high resolution and sensitivity enhancement. Operating at a wavelength of 790 nm, with a pulse energy of 4 nJ and a changeable power depending on the experiment, the laser was directed through a 40x objective lens to precisely target the intended cells. The ablation process followed meticulously drawn lines, and the QuantEM camera captured detailed images throughout the procedure [13].

2.2 Axonal Strength (Glucose Study)

Cortical neurons were collected from the cerebral cortex of P0 mouse pups cultured in Neurobasal A (GIBCO #11090-081) supplemented with 5% FBS Glutmax and B-27 supplements [19]. Cortical neurons were then treated with maintenance media (Neurobasal A, Glutmax, B27) containing either normal (3 mM) or high (25 mM) levels of glucose. After being cultured at these different glucose levels for about 40 minutes, the axons were damaged 20 microns away from the cell body, using the femtosecond laser at a power of 225-275 mw before the 40x objective. Phase images before and after laser ablation were collected at 5-minute intervals. Images were analyzed in ImageJ– the shrinkage created due to laser-inflicted damage was recorded in pixels, as demonstrated in Figure 1. The data of interest (pre-cut,

post 30 seconds, post 5 minutes, post 10 minutes, and post 15 minutes) were collected and grouped based on the medium the cells were cultured in (high glucose media and normal glucose media). The average length of the shrinkage was then calculated based on the post time

and graphed accordingly.

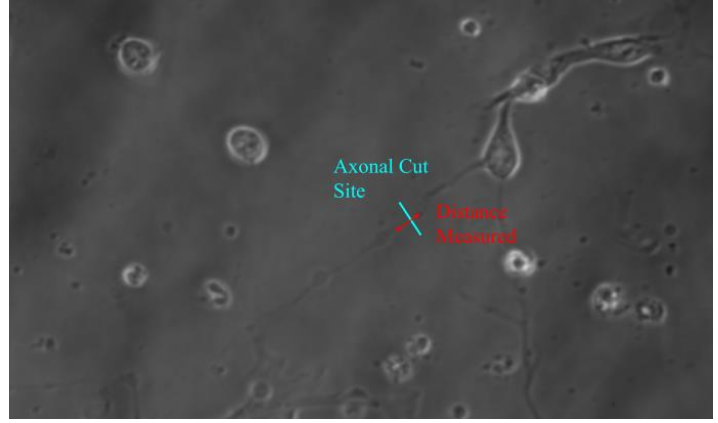


Figure 1. A sample cortical neuron with an axonal cut site (blue). The axonal strength was measured by the distance of the axonal gap (red).

2.3 Cardiomyocyte Study

The neonatal rat cardiomyocytes were isolated from hearts using the Worthington Neonatal Cardiomyocyte Isolation System [20]. The hearts were chilled and rinsed with CMF-HBSS and then refrigerated in 50 $\mu g/mL$ Trypsin. Twenty-four hours later, the tissue was warmed, oxygenated, and transferred into collagenase. Tubes were triturated to release cells and suspended and sedimented in Leibovitz L-15. Following a 4-day culture with a $2\mu g/cm^2$ fibronectin, the cells were stained with SYTOXTM Orange Nucleic Acid Stain twenty minutes before ablation.

Laser ablation patterns were drawn by hand using a custom-built Labview software, which when initiated, guided the laser through the triangular pattern drawn to ablate the cells. The power before the objective was measured to be 100 mW. An example of this can be seen in Figure 2. Laser ablation was able to replicate myocardial cell loss, creating an artificial border zone to replicate the effects on border cells from the loss of neighboring cells. The TrackMate-StarDist extension on ImageJ was used to create masks and collect the normalized area of border cells at frames before and after ablation. The border cells were marked with red tracks in the phase image (Figure 2). Through a MATLAB code, this data could then be assembled and graphed into several "tracks".

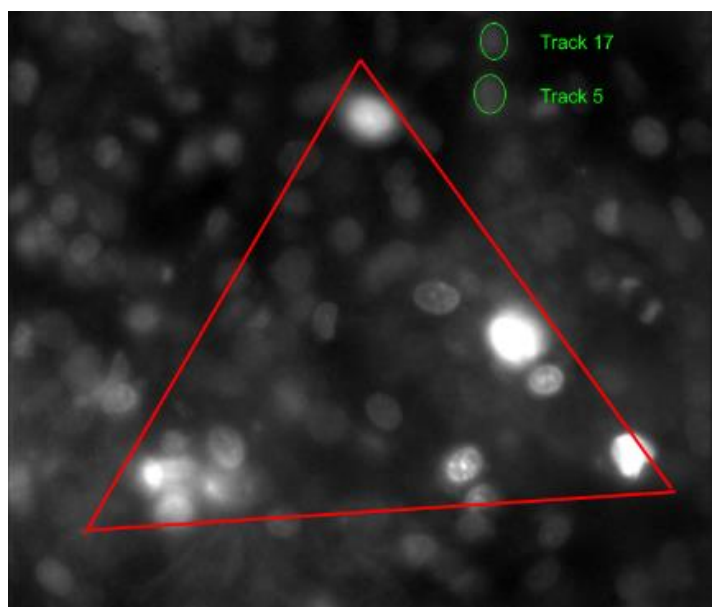


Figure 2. Phase image with indication of laser ablation area (triangle) and track indications (circles).

2.4 Quantitative Phase Imaging System

For PC-12 cells, the cover glasses were pre-coated with 0.1% PDL before plating. Then, the PC-12 cells were plated using DMEM high glucose, 1% penicillin/ streptomycin, 10% horse serum, and 5% fetal bovine serum. The cells were stored at 37°C in a 5% CO2 incubator. The quantitative phase imaging (QPI) methodology, FOSSMM, achieved 3D QPI to measure the the thickness. HEK 293 cells are grown on 60mm Nunc cell culture dishes (ThermoFisher) and in growth medium with 10% FBS and 1×Glutamax (Gibco, ThermoFisher), maintained at 37 °C and 5% CO2. 1-2 days before ablation, the cells were washed three times with Hanks Buffered Saline Solution ThermoFisher) devoid of calcium then gently detached with 1 mL of 1×TryplE Express Enzyme (Gibco, ThermoFisher) for 5 min, longer if detachment was not observed. Upon detachment, TryplE was quenched by the addition of 4 mL of growth medium, and the cells were then seeded onto imaging dishes [14].

For all experiments, the RoboLase system was used to image the cells in the XY plane. The ablation was carried out in a defined area and the resulting changes in thickness were captured using a QPI methodology named Fourier optical spin splitting microscopy (FOSSMM) [13]. FOSSMM consisted of two lenses, a metasurface, and a polarized camera, allowing for underfocused and overfocused images. The meta-device was 50 μm away from the flat surface of the substrate [21-22]. Imaging the same path was repeated at different

depths within the sample thickness by adjusting the position of the sample relative to the focusing arrangement along the beam propagation direction. Using the differences between the images, the QPI was acquired using the transport of intensity equation (TIE) algorithm[23] enabling real-time monitoring cell property changes. Our TIE-based reconstruction and metasurface optics are consistent with recent QPI/metasurface reports and design practice (single-shot amplitude/phase and compact meta-device implementations) [17].

2.5 Hippocampal Neuron Study (Huntington's Disease)

Wild-type and HD hippocampi were isolated from P0–P2 mouse pups, and the meninges were removed. The hippocampi were dissociated in a 0.5 mg/mL papain solution, incubated for 15 min, and washed with plating medium [24]. The dissociated hippocampal neurons were then either left untreated or treated with 1.5 mg or 3.0 mg nicotinamide (Ni) or with hydrogen peroxide (H_2O_2). Axons were ablated, and image sequences were acquired at 5-min intervals over 20 min. Axonal shrinkage was measured in ImageJ and analyzed as a function of time.

2.6 RGC Injury Model (Fluo-4 Calcium Imaging)

RGCs from postnatal day-5 Sprague-Dawley rats were purified by immunopanning, separated, and cultured in a serum-free defined medium supplemented with BDNF, CNTF, insulin, and forskolin. To monitor intracellular calcium, all RGCs were loaded with the Fluo-4 indicator 40 min before ablation. Dishes were placed on a microscope in phase-contrast mode, and coordinates of RGCs meeting selection criteria (relative isolation, a clearly defined axon, and minimal surrounding debris) were identified and recorded. The power before the objective was measured to be 250 mW. The epifluorescence arc lamp was set to 2% to minimize fluorescence variation from light exposure. Fluorescence images were then collected every 10 s for 5 min to obtain baseline signals. The axon of an individual cell in each field of view was ablated with a $275~\mu W$ laser positioned 20 μm from the soma (as shown in Figure 3), and imaging was continued at the same rate for an additional 5 min post-ablation. Four RGCs served as non-ablated controls and were imaged for 10 min under conditions. After identical acquisition, fluorescence intensities at the ablation site and at the soma were extracted in ImageJ and normalized to each

cell's pre-ablation median fluorescence to account for differences in starting luminosity.

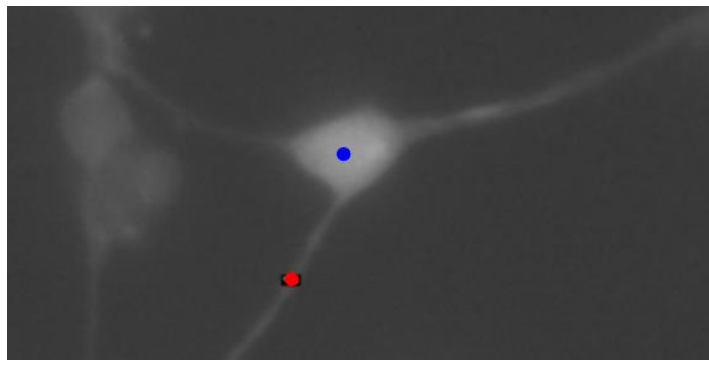


Figure 3. A sample RGC with the point of ablation highlighted in red. Fluorescence is measured at both the point of ablation (red) and the cell body (marked in blue).

3. Results and Discussion

3.1 Axonal Strength (Glucose Study)

Both high glucose and normal glucose (3 mM) showed clear signs of axonal damage after ablation (Figure 4). However, normal glucose (3 mM) neurons exhibited comparatively lower shrinkage than neurons in standard high glucose medium.

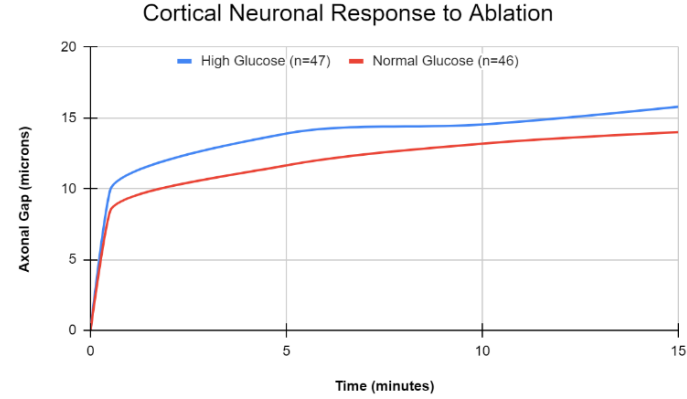


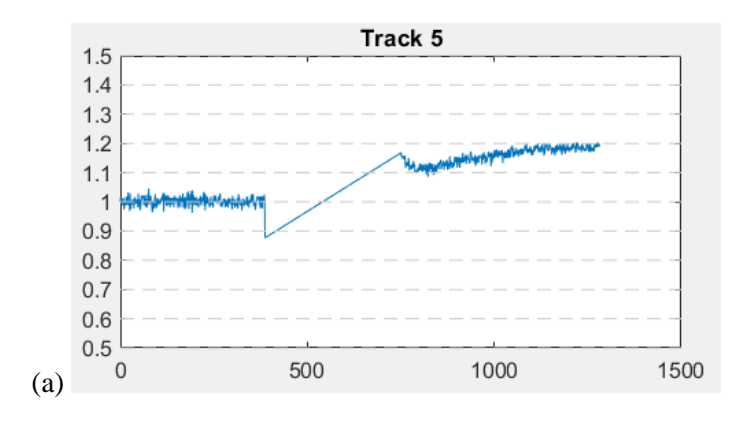
Figure 4. Graph of the axonal gap over time in response to ablation in cells with high glucose and normal glucose levels. High glucose: n = 47 cells; normal glucose: n = 46 cells.

Immediately after ablation, mean axonal shrinkage measured 9.9 μm under high glucose and 8.4 μm under normal glucose (3 mM). At 15 min post-ablation, shrinkage increased to 15.8 μm and 14.0 μm , respectively. Substantial variability was observed, with mean errors of 1.43 μm (high glucose) and 1.04 μm (normal glucose) at 15 min. With the available number of trials, a statistically significant difference between glucose conditions was not detected. Additional

experiments with larger sample sizes were judged necessary to determine whether the trend was robust. Nonetheless, the results indicated that laser ablation was a viable assay for probing axonal and neuronal robustness under differing extracellular conditions, including glucose levels.

3.2 Cardiomyocyte Study

More than 50 border cells outside the triangular ablation zone in Figure 2 were chosen and tracked before and after ablation as shown in Figure 5. Their areas before ablation were normalized to have an area of 1. Many of these border cells experienced changes after the ablation, with three sample tracks being shown below. After ablation, the cell marked as "Track 5" increased by 10% in area and continued to increase in area before reaching a maximum 20% increase. Similarly, tracks 17 and 19 demonstrated a 10% increase in area after ablation. Thus, by creating an artificial border zone with laser ablation, coupled image-tracking software can be used to ascertain changes in cellular shape, and thus the presence of irregular force and stress caused by the absence of neighboring cells. This opened many realms f possibilities when studying border zones caused by myocardial infarctions. For example, cells of different distances away from the border zone can be tracked separately to determine the effects of distance from the border zone on cellular stress.



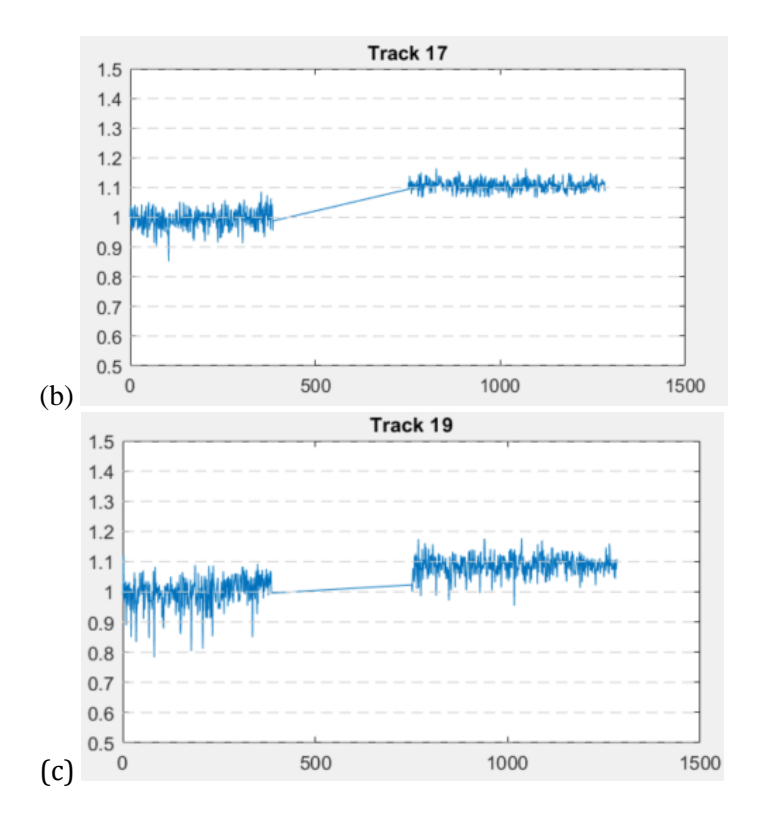


Figure 5. Measurements of normalized area of Heart Cells and the affected neighboring cells from various distances of the border zone. (a) Cellular Track 5 increases by 20% at the end of measurement. (b) Cellular Track 17 increases by 10% at the end of measurement. (c) Cellular Track 19 increases by 10% at the end of measurement.

The data proved that the loss of neighboring cells can indeed cause border cells to undergo changes. These irregular forces may play a large part in contributing to the growth of the border zone, as well as the development of cellular characteristics and niches specific to myocardial infarction cases. For future research, looking for patterns in the location of myocardial infarction relative to laser ablation by machine learning may make the spreading of border zones predictable. If the loss of neighboring cells was indeed due to mechanical stressors, the ability to predict which neighboring cells were susceptible to myocardial infarction expansion may allow for the development of treatments that stabilized heart tissue and neutralize mechanical stress before cell death by loss of neighboring cells occurs.

This laser ablation model also has a large potential for future improvement. For example, it could be possible to expand the simulation's scope by increasing the number of simulated cardiomyocytes and transitioning from a 2D grid to a full 3D tissue model.

This extension will enable a more accurate representation of scar formation and progression in a physiologically relevant context. This laser ablation model could also be used to investigate the role of rescue mechanisms during LON (loss of neighbor) events in the context of scar progression. The involvement of fibroblasts and macrophages and their potential rescue mechanisms can be explored within the simulation model. Interactions between cardiomyocytes, fibroblasts, and macrophages can also be incorporated to simulate the dynamic cellular crosstalk involved in scar formation and resolution.

3.3 Quantitative Phase Imaging (QPI) Study

In HEK293 cells, laser ablation caused a noticeable increase in cell thickness in areas surrounding the ablation region, suggesting a movement of cell mass within the cell. The phase imaging process allowed real-time visualization of these changes, something that may be important to future applications (Figure 6).

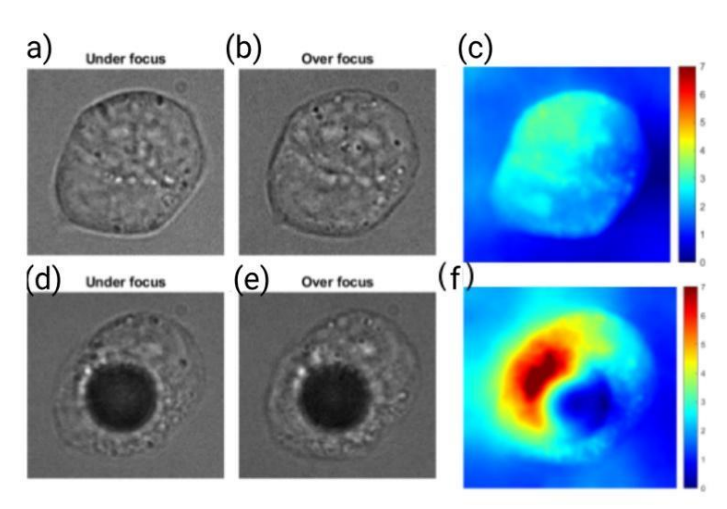


Figure 6. Phase images of HEK293 cells. (a) and (b) were the under focused and overfocused images after light passes through the meta-device for the cell before, (d) and (e) after ablation. (c) Image of the cell with thickness indicated before (f) being after laser ablation.

With PC-12, a different experimental process were implemented using different power levels and observing their correlated changes. Cell thickness was minimally impacted at the lowest power, 244 mW, with only a 0.50% change observed, shown in Figure 7A. This suggested that the laser energy was insufficient at this power level to induce significant structural alterations in the cells, likely because the energy absorbed was below the threshold needed to cause noticeable expansion

through the ablation. At a laser power of 281mW, a substantial increase in cell thickness was observed, with a 77.55% expansion occurring immediately after laser ablation, shown in Figure 7B. This change indicated that the laser power at this level was sufficient to induce damage, increasing cell volume, likely due to thermal effects or the generation of intracellular stress and swelling. The most pronounced effect was observed at the highest power, 311mW, where the cell thickness increased by 230.53% following laser ablation, shown in Figure 7C. This increase suggested a high degree of cellular disruption, potentially due to the formation of cavitation bubbles or other damage mechanisms induced by the higher energy input. The correlation in Figure 8 implied that as the laser power increased, the extent of cellular damage and subsequent expansion became more significant.

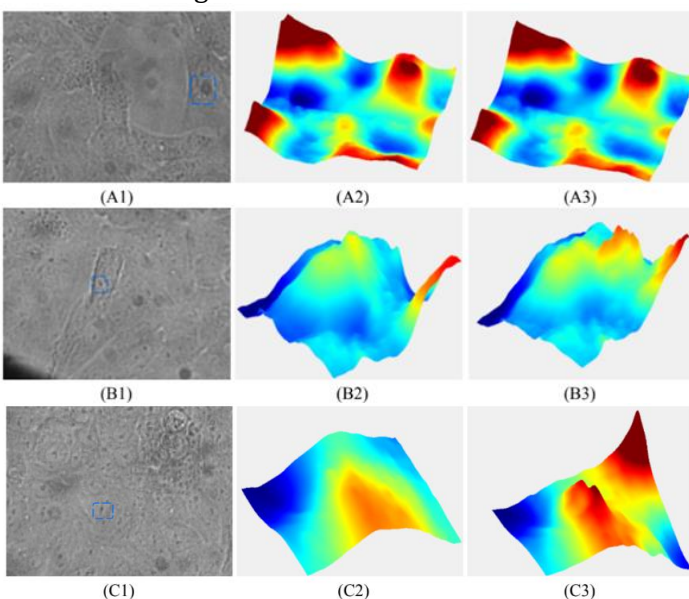


Figure 7. (A) 244 mW at focal plane was applied on the cell in the blue rectangle, (A1) Phase image, (A2) Thickness before laser ablation, (A3) Thickness right after laser ablation. (B) 281 mW at focal plane was applied, (B1) Phase image, (B2) Thickness before laser ablation, (B3) Thickness right after laser ablation. (C) 312 mW at focal plane was applied, (C1) Phase image, (C2) Thickness before laser ablation, (C3) Thickness right after laser ablation.

Effects of Ablation on Thickness of PC-12 Cells via Eagle-Eye Inspired Meta-Device

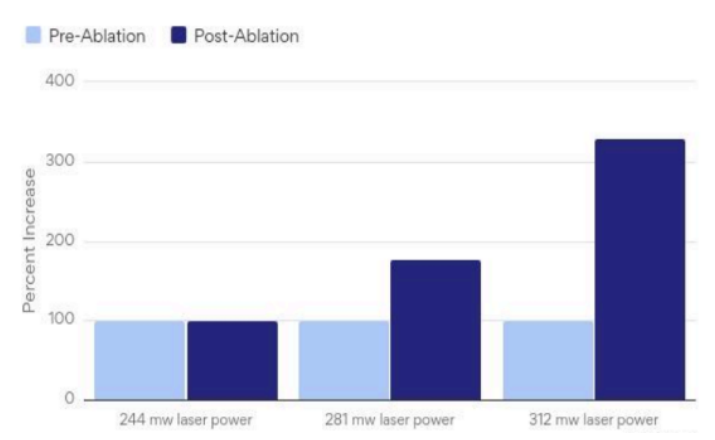


Figure 8. Thickness Change measured in correspondence to laser power, pre- and post-ablation of Figure 7.

In summary, these findings with PC-12 and HEK293 were crucial for understanding the effects of laser ablation on cellular structures. They informed future studies to optimize laser parameters for applications in cellular manipulation, laser surgery, and other biomedical fields. These observations align with emerging QPI literature where phase is sensitive to subcellular mass redistribution following perturbation [17].

3.4 Huntington's Disease

After analyzing the shrinkage of the axon post ablation for the nontreated HD and wild type hippocampal neurons, there was a greater amount of separation within the neurons affected by Huntington's Disease compared to the wild type neurons, however, there was no significant statistical difference between the separation (Figure 9). For the neurons treated with Ni, there was less degeneration in both wild type and HD cells, signalling that the axon was strengthened, with a greater effect observed in 3.0mg than the 1.5mg, shown in Figure 10. In the neurons treated with H_2O_2 , axonal degradation increased minimally, as seen in Figure 11.

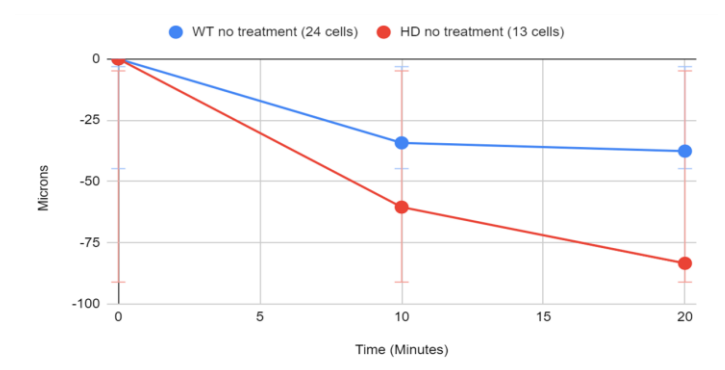


Figure 9. Graph of the axonal gap (microns) over time in response to ablation in wild type (blue) and HD hippocampal neurons.

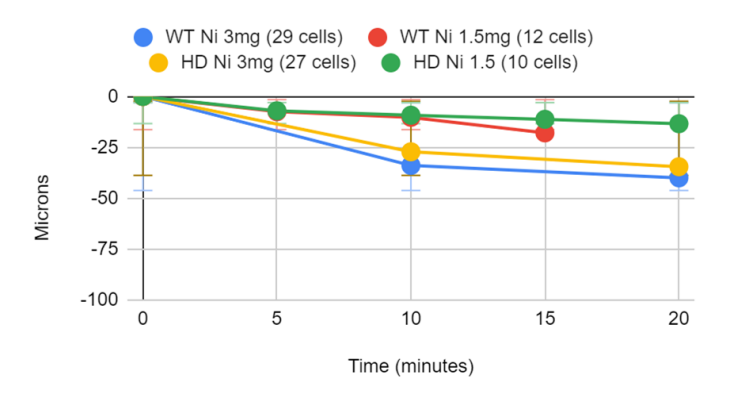


Figure 10. Graph of the axonal gap in wild type and HD neurons treated with 1.5mg and 3.0mg of Ni.

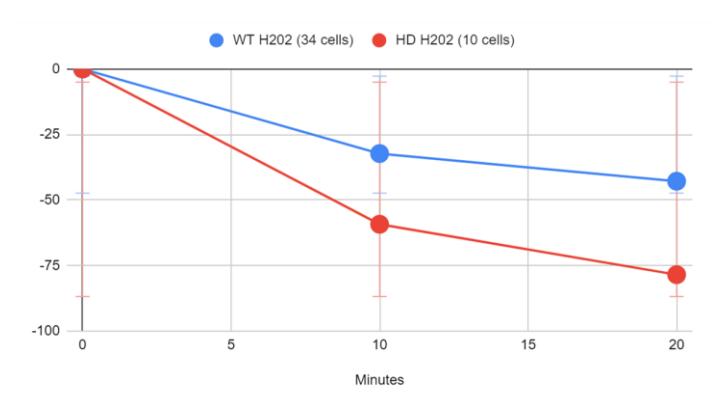


Figure 11. Graph of the axonal gap (microns) over time in response to ablation in wild type (blue) and HD hippocampal neurons treated with H₂O₂.

3.5 Retinal Ganglion Cells

After averaging the normalized fluorescence of the 15 ablated and 4 control cells' bodies and axons, the ablated cells' body and axon normalized fluorescence were compared with the control cells' body and axon normalized fluorescence. Both the cell body and axon had an immediate calcium response following ablation.

The ablated RGC cell somas had a peak average normalized fluorescence of 1.318 at approximately 45 seconds, while the ablated axons had a peak average normalized fluorescence of 1.049 at approximately 10 seconds. Both calcium fluorescence responded decreased exponentially after the spike. The average calcium fluorescence of the ablated RGC cell bodies dropped to 1.245 at 2 minutes, and 1.160 after 5 minutes. The average calcium fluorescence of the ablated RGC axons dropped to 1.021 at 2 minutes, and 1.013 after 5 minutes.

The fluctuation was observed in the form of a normal distribution in the fluorescence of separate neurons, with standard deviations for the cell soma of 0.1806 immediately after ablation and 0.167 after five minutes. Similarly, the axonal ablation model had standard deviations of .02593 immediately after ablation and .0246 after five minutes. Notably, Standard Mean Errors remained relatively low: .0466 in the cell body and .00670 in the axon ten seconds after ablation. This allowed for data sets (for example, between a treatment and wild type) of ablated cell somas and axons to be compared easily, and with statistical significance. RGCs were extremely light sensitive, and their calcium levels may fluctuate over time; therefore, a crucial part of the process was utilizing control RGCs to account for factors other than ablation. In both the cell body and axon, control fluorescence remained relatively stationary, ranging from 0.988 to 1.009 in the cell body, and 0.992 to 1.003 in the axon.

RGC calcium spikes were seen in the data in both the cell bodies and axons of ablated cells. By using control cell data, these fluorescence spikes were caused solely by the laser ablation, and not by outside factors such as arc lamp light exposure. The axons displayed an immediate calcium fluorescence spike, while the cell bodies exhibited a delayed spike with a larger average magnitude. After the peak, calcium-induced fluorescence decreased exponentially in both the cell body and the axon but stayed at relatively high levels (compared to before ablation) in the five minutes post-ablation. Although solely wild-type RGCs and their cell body and axonal calcium responses were tested with respect to ablation, the laser ablation and fluorescence imaging combination could potentially be utilized to test neurodegenerative treatments such as some drugs, gene therapies, or knockdown/overexpression of certain genes. The same system could be used to measure changes in calcium signal after an injury model made by a laser. The calcium fluorescence measurements had relatively low standard deviations and errors in the mean, and these fluctuations showed a decrease as time increased after ablation. This suggested that the laser ablation model would be a good candidate to quickly and efficiently measure differences in neural responses, potentially between wild-type RGCs and RGCs treated by therapies or drugs.

4. Conclusion

We integrated a RoboLase-QPI workflow that pairs controlled femtosecond laser perturbations with quantitative, label-free readouts, creating a practical platform for mechanism-driven therapeutic screening. Beyond methodological value, each model maps to a translational use case: glucose modulation and axonal stability for diabetic neuropathy; border-zone mechanics after focal injury for cardiac remodeling; quantitative injury readouts to assess neuroprotectants in Huntington's disease; and axonal/somatic Ca2+ signatures as biomarkers in glaucoma. A subset of results—specifically the glucose comparison in cortical neurons and the cardiomyocyte border-zone analysis should be regarded as preliminary due to limited biological replication; we outline powered confirmation experiments in the next-steps section. Near-term priorities include higher-NA confirmation, standardized thermometry and fiducial-based registration, expanded biological replicates, and open sharing of analysis code/ROI masks. Collectively, these steps position the approach to shorten iteration cycles between hypothesis, perturbation, and quantitative readout, accelerating early translational testing across neurological and cardiac indications.

5. Acknowledgements

We would like to thank Dr. Kevin King's lab for providing the heart. This material was based upon work supported by a gift from Beckman Laser Institute Inc. to L.S. and V.G.G. Special thanks to the private donors to our UCSD IEM BTC center: Dr. Shu Chien from UCSD Bioengineering, Dr. Lizhu Chen from CorDx Inc., Dr. Xinhua Zheng, David & Leslie Lee, Mingwei Hu and Wen Shi for their generous donations.

References

- [1] M. W. Berns, "Laser scissors and tweezers," *Scientific American*, vol. 278, no. 4, pp. 62–67, Apr. 1998, doi: 10.1038/scientificamerican0498-62.
- [2] H. Zhang, Y. Li, S. B. Shah, S. Li, Q. Li, J. Oaks, T. Lv, L. Z. Shi, H. Wang, D. Wang, X. Wu, "ATM

- priming and end resection-coupled phosphorylation of MRE11 is important for fork protection and replication restart," Proc Natl Acad Sci U S A. 2025 Apr 22;122(16):e2422720122. doi: 10.1073/pnas.2422720122. Epub 2025 Apr 18. PMID: 40249789; PMCID: PMC12037065.
- [3] T. Wu, Y. Li, Y. Zhao, S. B. Shah, L. Z. Shi, X. Wu, "Break-induced replication is activated to repair R-loop-associated double-strand breaks in SETX-deficient cells," Cell Rep. 2025 Sep 30;44(10):116386. doi: 10.1016/j.celrep.2025.116386. Epub ahead of print. PMID: 41037402.
- [4] S. B. Shah, Y. Li, S. Li, Q. Hu, T. Wu, Y. Shi, T. Nguyen, I. Ive, L. Shi, H. Wang, X. Wu, "53BP1 deficiency leads to hyperrecombination using breakinduced replication (BIR)," Nat Commun. 2024 Oct 5;15(1):8648. doi: 10.1038/s41467-024-52916-z. PMID: 39368985; PMCID: PMC11455893.
- [5] L. Jia, L. Wang, M. Chopp, Y. Zhang, A. Szalad, and Z. G. Zhang, "MicroRNA 146a Locally Mediates Distal Axonal Growth of Dorsal Root Ganglia Neurons under High Glucose and Sildenafil Conditions," *Neuroscience*, vol. 329, pp. 43–53, Aug. 2016, doi:10.1016/j.neuroscience.2016.05.005.
- [6] M. Saleh and J. A. Ambrose, "Understanding Myocardial Infarction," *F1000Research*, vol. 7, no. 1, p. 1378, Sep. 2018, doi: 10.12688/f1000research.15096.1.
- [7] K. R. King, D. M. Calcagno, N. Taghdiri, A. Toomu, V. Ninh, and Z. Fu, "SINGLE CELL AND SPATIAL TRANSCRIPTOMICS OF THE ISCHEMIC BORDERZONE," *Journal of the American College of Cardiology*, vol. 79, no. 9, p. 971, Mar. 2022, doi: 10.1016/S0735-1097(22)01962-3.
- [8] M. J. Berridge, P. Lipp, and M. D. Bootman, "The Calcium Entry Pas de Deux," *Science*, vol. 287, no. 5458, pp. 1604–1605, Mar. 2000, doi: 10.1126/science.287.5458.1604.
- [9] N. Yu, P. Genevet, M. Kats, F. Aieta, J. P. Tentienne, F. Capasso, and Z. Gaburro, "Light Propagation with Phase Discontinuities: Generalized Laws of Reflection and Refraction," *Science*, vol. 334, no. 6054, pp. 333–337, Sep. 2011, doi: 10.1126/science.1210713.
- [10] J. Zhou and Z. Liu, "Photonic spin-dependent wave shaping with metasurfaces: applications in edge detection," *Plasmonic Materials and Metastructures*, pp. 227–243, Sep. 2023, doi: 10.1016/b978-0-323-85379-8.00008-3.

- [11] T. J. Cui, S. Zhang, A. Alù, M. Wegener, J. Pendry, J. Luo, Y. Lai, Z. Wang, X. Lin, and H. Chen, "Roadmap on electromagnetic metamaterials and metasurfaces," *Journal of Physics: Photonics*, vol. 6, no. 3, p. 032502, Jan. 2024, doi: 10.1088/2515-7647/ad1a3b.
- [12] W. Yang, J. Zhou, D. P. Tsai, and S. Xiao, "Advanced manufacturing of dielectric metadevices," *Photonics Insights*, vol. 3, no. 2, p. R04, Jan. 2024, doi: 10.3788/pi.2024.r04.
- [13] J. Zhou, Q. Wu, J. Zhao, C. Posner, M. Lei, G. Chen, J. Zhang, and Z. Liu, "Fourier Optical Spin Splitting Microscopy," *Physical Review Letters*, vol. 129, no. 2, Jul. 2022, doi: 10.1103/physrevlett.129.020801.
- [14] J. Zhou, F. Tian, J. Hu, L. Z. Shi, V. G. Godinez, D. P. Tsai, and Z. Liu, "Eagle-Eye Inspired Meta-Device for Phase Imaging," *Advanced Materials*, vol. 36, no. 32, p. 202402751, Jun. 2024, doi: 10.1002/adma.202402751.
- [15] Q. Wu, J. Zhou, X. Chen, J. Zhao, M. Lei, G. Chen, Y. Lo, and Z. Liu, "Single-shot quantitative amplitude and phase imaging based on a pair of all-dielectric metasurfaces," *Optica*, vol. 10, no. 5, p. 619, Apr. 2023, doi: 10.1364/optica.483366.
- [16] Y. Liu, Y., W. Li, M. Ji, Y. Zhang, X. Ma, Z. Liu, X. Weng, "Biopsy of Porcine Blastocysts for Sex Identification and Transcriptome Sequencing Based on Laser-Assisted Microdissection," Reprod Domest Anim. 2025 Jun;60(6):e70087. doi: 10.1111/rda.70087. PMID: 40495623.
- [17] Y. Lian, Y. Liu, D. Cheng, C. Chi, Y. Bao, Y. Wang. "Dual-mode varifocal Moiré metalens for quantitative phase and edge-enhanced imaging." Nanophotonics. 2025 Aug 6;14(18):3053-3062. doi: 10.1515/nanoph-2025-0245. PMID: 40970243; PMCID: PMC12442366.
- P. Wang, J. Liang, L. Z. Shi, Y. Wang, P. Zhang, M. [18] Ouyang, D. Preece, Q. Peng, L. Shao, J. Fan, J. Sun, S. S. Li, M. W. Berns, H. Zhao, and Y. Wang, "Visualizing Spatiotemporal **Dynamics** of Intercellular Mechanotransmission upon Wounding," ACS photonics, vol. 5, no. 9, pp. 3565-3574, Aug. 2018, doi: 10.1021/acsphotonics.8b00383.
- [19] L. G. W. Hilgenberg and M. A. Smith, "Preparation of Dissociated Mouse Cortical Neuron Cultures," *Journal of Visualized Experiments*, vol.562, no. 10, Dec. 2007, doi: 10.3791/562.
- [20] "Neonatal cardiomyocyte Isolation System -Worthington Enzyme Manual," Worthington Biochemical. Available: https://www.worthington-

- biochem.com/products/neonatal-cardiomyocyte-isolation-system/manual
- [21] J. Zhou, H. Qian, H. Luo, S. Wen, and Z. Liu, "A spin controlled wavefront shaping metasurface with low dispersion in visible frequencies," *Nanoscale*, vol. 11, no. 36, pp. 17111–17119, Jan. 2019, doi: 10.1039/c9nr03566d.
- [22] J. Zhou, H. Qian, G. Hu, H. Luo, S. Wen, and Z. Liu, "Broadband Photonic Spin Hall Meta-Lens," *ACS Nano*, vol. 12, no. 1, pp. 82–88, Dec. 2017, doi: 10.1021/acsnano.7b07379.
- [23] J. Zhang, Q. Chen, J. Sun, L. Tian, and C. Zuo, "On a universal solution to the transport-of-intensity equation," *Optics Letters*, vol. 45, no. 13, pp. 3649-3652, Jun. 2020, doi: 10.1364/ol.391823.
- [24] "Cell Press: STAR Protocols." https://star-protocols.cell.com/protocols/3407#bib1